Feasibility of Electron Bernstein Wave Coupling via O-X-B Mode Conversion in the RFX–mod reversed field pinch device

R. Bilato[1], F. Volpe[1], A. Köhn[2], R. Paccagnella[3,4], D. Farina[5], E. Poli[1], M. Brambilla[1]

[1] Max–Planck Institut für Plasmaphysik – EURATOM Association – Garching, Germany
[2] Institut für Plasmaforschung, Universität Stuttgart - Germany
[3] Consorzio RFX – Associazione EURATOM sulla fusione – Padova, Italy
[4] Consiglio Nazionale delle Ricerche, Italy
[5] IFP-CNR, EURATOM-ENEA-CNR Association – Milano, Italy

E-mail: `roberto.bilatoatipp.mpg.de`

Abstract. Electron Bernstein wave coupling through the Ordinary-eXtraordinary-Bernstein (O-X-B) scheme has been modelled for RFX-mod overdense plasmas. The compromise between constraints from plasma parameters and from a viable launcher design highlights the commercial frequency of 28 GHz as a promising candidate. At this frequency a steerable quasi–optical launch system has the flexibility necessary for tuning the optimal operational window for the O-X mode conversion. According to the results of a two-dimensional full-wave code [A. Köhn el al. Plasma Phys. Control. Fusion **50** (2008)085018], the maximum O-X mode conversion efficiency amounts to 58 % for a single pass.

1. Introduction

The Reversed Field Pinch (RFP) configuration is made possible by a dynamo mechanism which converts poloidal to toroidal magnetic flux. This flux–conversion mechanism is sustained by current -driven tearing instabilities, which, however, are also often responsible for magnetic field stochastization and transport degradation. Significant improvements have been recently obtained in the RFX-mod device with an extended set of active control coils [1]. Improvements of RFP plasma performances were also achieved by active inductive–control of the poloidal current (pulsed poloidal current drive – PPCD) [2, 3]. A flexible and efficient current profile control scheme could reconcile the scaling laws of the ordinary turbulent RFP with reactor relevant-regimes by drastically reducing the dynamo fluctuations [4]. In particular, an adjustable radio-frequency (rf) heating and current drive system can provide some degree of flexibility in controlling the current profile around the reversal of the toroidal component of the confining magnetic field.

In the past, the attention in the RFP community has been paid mainly to waves in the Lower Hybrid range of frequencies [5], which have a marginal operation window in the Reversed Field eXperiment (RFX) [6]. Similarly, traditional electron cyclotron resonance heating (ECRH) schemes based on the launch and direct absorption of 1$^{\text{st}}$ harmonic O–mode and 2$^{\text{nd}}$ harmonic X–mode suffer from severe wave accessibility constraints in RFPs which typically operate with overdense plasmas ($\omega_{\text{pe}}/\Omega_{\text{ce}} \gg 1$), except for a thin layer at the edge. Hereafter and in the remainder $\omega_{\text{pe}} = (e^2 n_e/(\epsilon_0 m_e))^{1/2}$ is the electron plasma (angular) frequency and $\Omega_{\text{ce}} = e B/m_e$ the electron cyclotron (angular) frequency.

In spite of this, recent measurements on MST of ECRF emission of the X– and O–mode, explainable in terms of electron Bernstein waves (EBW) born in the plasma core [7], have triggered an interest in EBW applications to heating and current drive in RFPs [8], on the basis of the principle of reciprocity. Once EBWs are excited, they are efficiently absorbed close to the electron cyclotron harmonics and their current drive (CD) efficiency is predicted [9, 10] and experimentally confirmed [11] to be higher than the traditional EC schemes. The main issue with these waves is how to excite them inside the plasma. The EBWs are efficiently excited via mode conversion of the slow X-mode at the upper-hybrid resonance (UHR) ($\omega_{\text{UH}}^2 = \omega_{\text{pe}}^2 + \Omega_{\text{ce}}^2$). The most straightforward scheme is to launch X waves which are mode converted in EBWs at the UHR. With the antenna on the low-field side this scheme suffers from the serious limitation of the evanescence layer between the X-cutoff (right cutoff $\omega_{\text{R}} = \sqrt{4\,\omega_{\text{pe}}^2 + \Omega_{\text{ce}}^2}/2 + \Omega_{\text{ce}}/2$) and the UHR. In Tokamaks [12, 13] and Stellarators [14], the X-mode does not encounter cutoffs up to the UHR if launched from the high field sides. However, as discussed later, RFPs cannot take advantage of the high-field-side launch of the X wave. An alternative scheme in overdense plasma, experimentally verified for Stellarators [15] and for Tokamaks [16] is the double O-X-B mode conversion: the O wave launched from the low field side with an optimal angle is mode converted into an X wave at the O-mode

cutoff layer ($\omega = \omega_{\rm pe}$). In turn the X-mode converts into the EBW at the UHR.

In this study we investigate the frequency and angular operational windows for these schemes in RFX-mod as a first step of the feasibility study of an ECCD system. A detailed analysis of the CD efficiency theoretically achievable for typical RFX-mod plasma parameters will be addressed in the future. In the next Section we discuss the X-B and O-X-B schemes paying particular emphasis on the RFP peculiarities. We will see that in the case of RFX-mod at plasma currents of the order of MA, the only viable scheme is the O-X-B one. In Section 3 we identify a RFX-mod port suitable for the injection of a Gaussian beam of microwaves and discuss the best geometry for OXB conversion. Finally in Section 4 we quantify the O-X mode conversion efficiency at the P cutoff with the full–wave code IPF-FDMC [17]. The mode conversion X-B at the UHR can also be addressed with the IPF-FDMC code.

2. EBW in RFPs

2.1. Equilibrium and profiles

For a parametric study we consider analytical equilibria and we assume the following electron density and temperature dependences on the radial coordinate normalized to the minor radius a:

$$n(x) = n_0 \left[1 - \left(\frac{x}{x_{\rm LCFS}\, \eta_n} \right)^{\alpha_{ni}} \right]^{\alpha_{ne}} \quad \text{with} \quad \eta_n^{-1} = \left[1 - \left(\frac{n_{\rm LCFS}}{n_0} \right)^{1/\alpha_{ne}} \right]^{1/\alpha_{ni}} \quad (1)$$

$$T(x) = T_0 \left[1 - \left(\frac{x}{x_{\rm LCFS}\, \eta_T} \right)^{\alpha_{Ti}} \right]^{\alpha_{Te}} \quad \text{with} \quad \eta_T^{-1} = \left[1 - \left(\frac{T_{\rm LCFS}}{T_0} \right)^{1/\alpha_{Te}} \right]^{1/\alpha_{Ti}} \quad (2)$$

with $x_{\rm LCFS} < 1$ the position of the last closed flux surface (LCFS). The density on axis is $n_0[{\rm m}^{-3}] = I_p/[(I/N)\,\pi a^2]$ and the temperature is determined from the scaling of $\beta = 6.20 \cdot 10^{-12}\, (I/N)^{-0.73}$ [18]. For RFX-mod the minor radius a is 0.46 m and I/N is a typical RFP plasma parameter expressed in 10^{-14} A m with N the linear density and $I \equiv I_p$ the total plasma current. The density and temperature at the LCFS are assumed to be one tenth of the corresponding values on axis and the exponents are $\alpha_{ne} = \alpha_{Te} = 1$, $\alpha_{ni} = 6$ and $\alpha_{Ti} = 3$. In addition, we consider a scrape–off layer ($x_{\rm LCFS} < x < 1$) with an e-folding density profile

$$\ln \left(\frac{n_{\rm SOL}(x) + -\tilde{n}}{n_{\rm LCFS} + \tilde{n}} \right) = -\frac{x - x_{\rm LCFS}}{\gamma + (\xi - \gamma)(x - x_{\rm LCFS})/(1 - x_{\rm LCFS})} \quad (3)$$

where:

$$\tilde{n} = n_{\rm LCFS}\, \frac{e^{-(1-x_{\rm LCFS})/\xi}}{1 - e^{-(1-x_{\rm LCFS})/\xi}} \quad (4)$$

$$\gamma = \frac{n_{\rm LCFS} + \tilde{n}}{n_0}\, \frac{x_{\rm LCFS}\, \eta}{\alpha_{ni}\, \alpha_{ne}\, (1 - \eta^{\alpha_{ni}})^{\alpha_{ne}-1} \eta^{1-\alpha_{ni}}} \quad (5)$$

The density profile starts from zero (vacuum) with an e-folding equal to ξ and matches with continuity the inner density profile at $x_{\rm LCFS}$. We assume $(1 - x_{\rm LCFS})\, a \approx 5\,\lambda_0$, with $\lambda_0 = c/f$ the wavelength in vacuum.
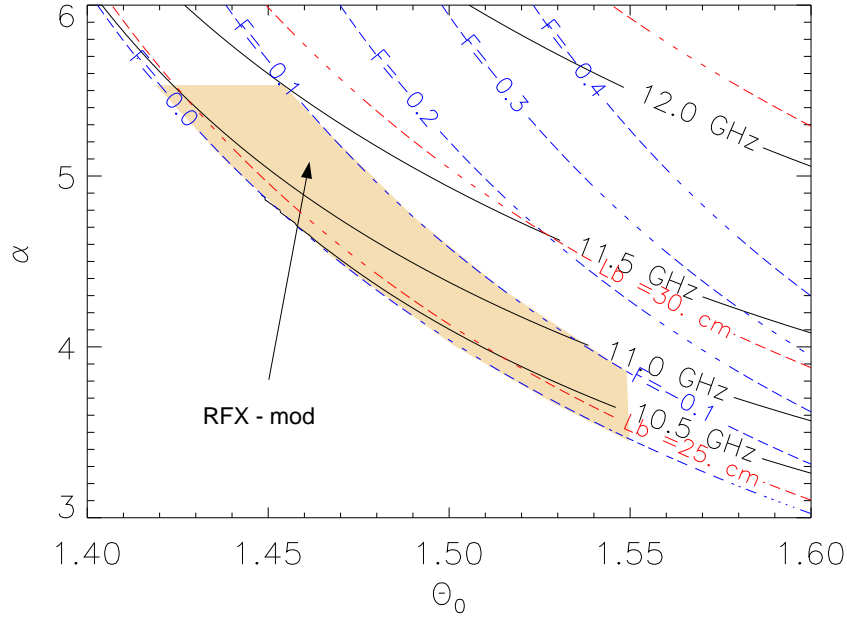
Figure 1. f_{ce} at the reversal layer for RFX-mod and at 1 MA of plasma current as function of the equilibrium parameters (α, Θ_0) of (6). The dashed lines are the contour levels of the reversal parameter F, defined as $B_\phi(x = 1)$ normalized to the total toroidal magnetic flux. The dotted lines are the values of $L_B = B/(\partial B/\partial x)$ at the reversal.

For the profiles of the poloidal and toroidal components of the confining magnetic field, B_θ and B_φ, we adopt a simplified version of the $\mu \& p$ model [19], which still reproduces finite pressure effects:

$$B_\varphi = B_0 \, J_0(f(x))$$

$$B_\theta = B_0 \, g(x) \, J_1(f(x)) \tag{6}$$

with $f(x) = \int \mu(x')\mathrm{d}x'$, $\mu(x) = 2\Theta_0 \, (1 - x^\alpha)$, $g(x) = f(x)/(2\Theta_0 \, x)$ and $B_0 = \mu_0 I_p/(\pi a)$. $J_{0,1}$ are the Bessel functions of the first kind of order 0 and 1. The parameters Θ_0 and α of the model are such that Eq. (6) describes tokamak equilibria for $\alpha, \Theta_0 \ll 1$ and RFP equilibria for $\alpha, \Theta_0 > 1$. Figure 1 shows the electron cyclotron frequency f_{ce} and the reversal parameter F at the reversal layer as functions of the parameters (α, Θ_0) of Eq. (6). The values in Fig. (1) are obtained for a plasma current $I_p = 1$ MA and they scale linearly with I_p. Hereafter, we make use of the dimensionless density $X = \omega_{pe}^2/\omega^2$ and magnetic field $Y = \Omega_{ce}/\omega$, where $\omega = 2\pi f$ is the angular frequency of the injected waves. We recall that $X \approx a^2 \, n_e/f^2$ and $Y = a \, B/f$ with $a \approx 28$, if the magnetic field B, the plasma density n_e and the wave frequency f are expressed respectively in Tesla, 10^{19} m^{-3} and GHz.
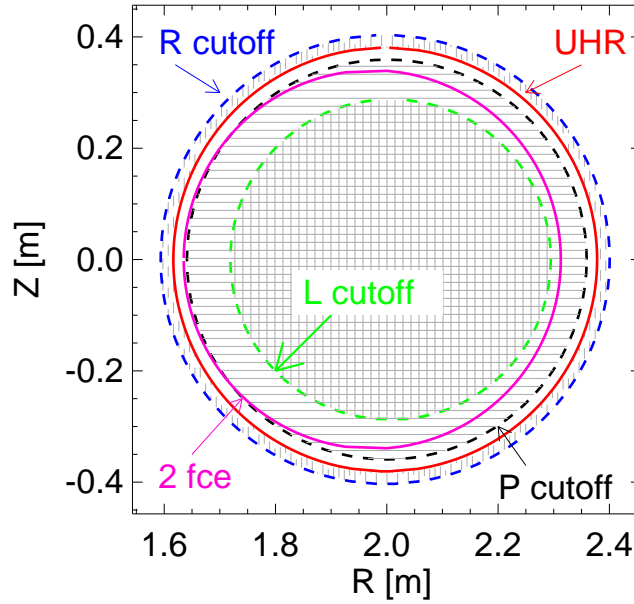
Figure 2. Position of resonances (solid) and cutoffs (dashed), in Stix's notation, in a poloidal section of RFX-mod for $f = 2\,f_{ce} = 28$ GHz, $I_p = 1$ MA, $n = 2.5 \cdot 10^{19}$ m^{-3} (in Stix's notation). Vertically (horizontally) hatched regions are not accessible respectively to X O mode.

2.2. EBW scenarios

In the frame of EC wave propagation, RFP plasmas are peculiar for at least three aspects.

First, like spherical Tokamaks, several Stellarators and some Tokamaks, RFP plasmas are overdense, i.e. $\sqrt{X} > Y$. This narrows the operation window for direct 2nd harmonic X-mode heating (i.e. without tunneling through evanescence regions). A larger operative window is available for 2nd harmonic O-mode heating. However, this scheme suffers from low absorption, which not only makes the scheme inefficient but might overload the first wall.

The second characteristic is that the module of the confining magnetic field is almost poloidally symmetric. Therefore the resonance and cutoff layers are almost circular and centered at the magnetic axis, as shown in Fig. (2). It follows that any launching position (including the inboard side of the device) is inherently "low field side". Thus, a "high field side" scheme, such as the slow X–B mode conversion, is not applicable to RFPs.

The third peculiarity of RFP plasmas is the low confining magnetic field which obliges to work at low frequencies to have low EC harmonics (the 1st and the 2nd) inside the plasma.

Since the driven current should be around the reversal of the toroidal component of the magnetic field, the cyclotron resonance has to lie not too far from the plasma edge.
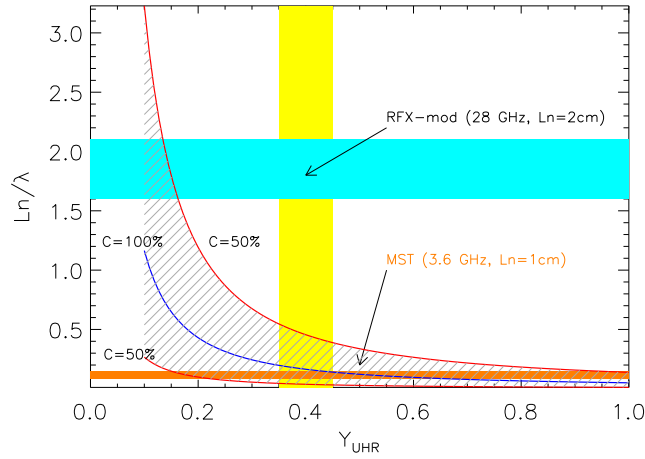
Figure 3. Optimal parameter region for X-O power transfer (larger than 50%) in terms of L_n/λ and Y at the UHR. The yellow rectangular highlights where the Y should be for ECCD.

In addition, due to the active control coils installed in RFX, plasma currents larger than 1 MA are routinely achieved. Thus, as shown in Fig. 2, a reasonable compromise is to operate with a commercial 28 GHz source at the 2nd harmonic. Hereafter, we will specialize the results to this frequency, trying, however, to keep them general, whenever possible.

An EBW system based on the launch of the X waves from the low field side has been realized at MST [8]: the launched X wave tunnels through the evanescence layer and is partially mode converted in EBWs at the UHR ($X = 1 - Y^2$). This scheme recalls the IBW excitation in the so-called mode conversion regime in the Ion Cyclotron range of frequencies. The conversion factor is $C = 4 \exp(-\eta_X) [1 - \exp(-\eta_X)]$ with the Budden parameter η given by [20]:

$$\eta_X \approx 2\pi^2 \, \frac{L_n}{\lambda} \, Y \, \sqrt{\frac{Y}{1+Y}} \tag{7}$$

and $\lambda = c/f$ the vacuum wavelength (≈ 1 cm for $f = 28$ GHz). Equation (7) holds in the limit $L_B \gg L_n$, with $L_n = n/(\partial n/\partial x)$ and $L_B = B/(\partial B/\partial x)$ respectively the density and magnetic field scale lengths. If $L_n \gg \lambda$ the evanescence layer is too large for the wave to tunnel through it. However, if $L_n \ll \lambda$ the waves encounters a sharp transition of the refraction index which causes a reflection. Typical values of L_B are shown in Fig. (1), whereas L_n in RFX is approximately 2 cm for I_p up to 0.8 MA [21]. In Fig. (3) the solid line shows L_n/λ as function of Y_{UH} (value of Y at UHR) for the 100% X-B conversion. The dashed region corresponds to $C > 50\%$. The vertical strip highlights the Y value region with power absorption near the reversal and the horizontal strips are the operational windows for 28 GHz (RFX-mod) and for 3.6 GHz (MST), the latter calculated assuming $L_n = 1$ cm [8]. Because of the short wavelength, the X-B scenario must be discarded in high current RFX-mod plasmas.
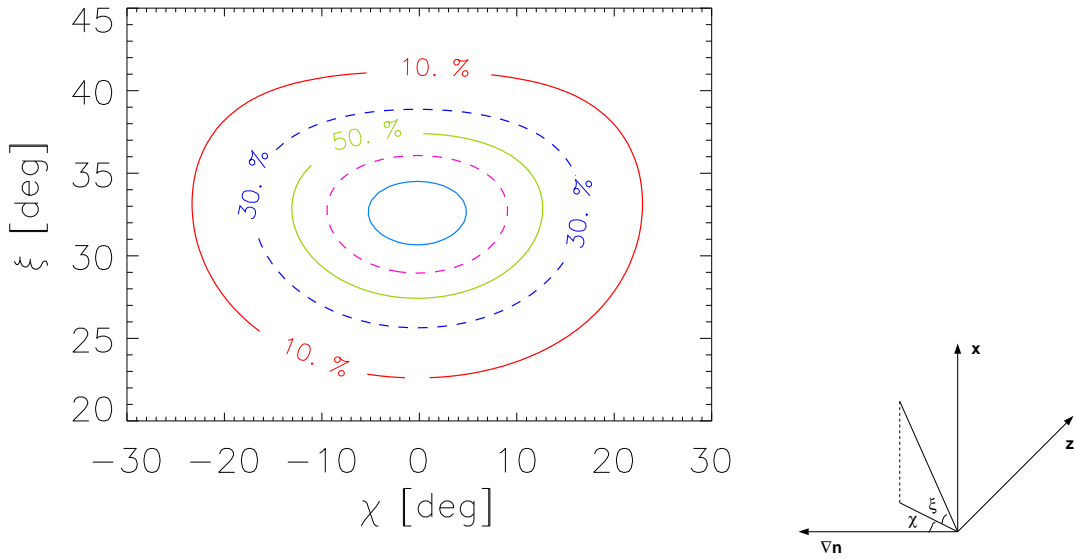
Figure 4. Transmission coefficients as function of the launch angles (ξ, χ). ξ is the elevation angle with respect to the middle plane and χ the angle formed with the toroidal direction (see the inset). This case refers to $(\alpha = 5.1, \Theta_0 = 1.47)$, $I_p = 1$ MA, $I/N = 7 \cdot 10^{-14}$ A m $(n_0 = 2.5 \cdot 10^{19}$ m$^{-3})$

In the O-X-B double mode conversion process, proposed by Preinhaelter and Kopecky [22], the O-wave, launched from the low field side with an optimal angle, propagates up to the O-mode cutoff layer $(X = 1)$ where it is mode converted in the X-slow wave with the following power transmission function $T(n_\perp, n_\parallel)$ [23]

$$T(n_\perp, n_\parallel) = \exp\left\{ -2\pi^2 \frac{L_n}{\lambda} \sqrt{\frac{Y}{2}} \left[2(1+Y)(n_{\parallel,\text{opt}} - n_\parallel)^2 + n_\perp^2 \right] \right\} \qquad (8)$$

where $n_\parallel$ and $n_\perp$ are respectively the parallel and perpendicular (with respect to the confining magnetic field) components of the refractive index vector $\vec{n} = \vec{k}/k_0$, with $k_0 = 2\pi/\lambda$. L_n and Y are evaluated at the conversion layer. The optimal launch angle is defined by the condition $n_\parallel^2 = n_{\parallel,\text{opt}}^2 = Y/(Y + 1)$ at the O-cutoff, i.e. the condition of O-mode cutoff $(X = 1)$ merging in the L-cutoff $(L = n_\parallel^2 \longrightarrow X = (1 - n_\parallel^2)(1 + Y))$. Figure 4 shows the contour levels of the transmission function (8), calculated in slab geometry as a function of the launching angles ξ and χ, respectively the elevation angle with respect to the middle plane and the angle with the toroidal direction. The extent of the ellipse axis depends on L_n/λ, whereas the ellipticity on $2(1 + Y_{\text{UHR}})$. Thus, the tolerance in the launch angle with respect to the optimal value depends strongly on L_n/λ, being higher for steeper density profiles. On the other hand, excessively steep density gradients can lead to high wave reflection, but this is not the case for 28 GHz in RFX-mod.

A first operational constraint of this scheme is that the O-mode cutoff must fall inside the plasma $(X_0 > 1$, with X_0 at the highest density). In addition, to be efficiently
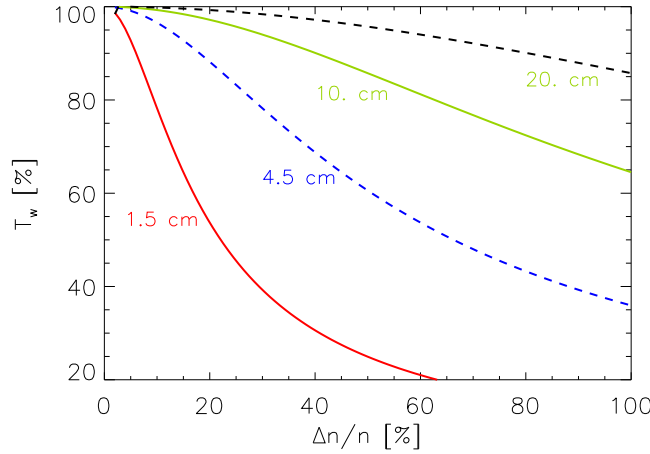
Figure 5. Transmission coefficient for optimal launch conditions in presence of density fluctuations, for three different correlation lengths.

absorbed, the EBW has to cross an electron cyclotron harmonics in its propagation from the UHR towards the high density plasma core, i.e. $X_p > X_{\text{UHR}} \equiv (p^2 - 1)/p^2$ with p the harmonics order ($\omega = p\Omega_{\text{ce}}$). We re-write this constraints as $b\, X_p > (p^2 - 1)/p^2$ where b is the plasma density at the pth cyclotron harmonic resonance as a fraction of the density on the axis n_0. Expressing the central density as a function of I_p and I/N as done after Equations (1,2) and assuming $p = 2$, the operational regime at 28 GHz and $I_p \approx 1$ MA is $I/N < 20\, b$. Since usually $b < 0.5$ this constraint allows a reasonable operational window in terms of I/N.

Another important issue in the O-X mode conversion is the influence of density fluctuations on the transmission. Following the approach of Ref. [15], the effects of density fluctuations on the toroidal component n_z of the refractive index are described by a probability density function,

$$p(n_z) = \frac{\lambda_z}{\sqrt{2\pi}\,\sigma_x}\, \exp\left(-\frac{n_z^2\,\lambda_z^2}{2\,(1 - n_z^2)\,\sigma_x}\right)\left(1 - n_z^2\right)^{-3/2} \tag{9}$$

with λ_z the toroidal characteristic correlation length and $\sigma_x = L_n\,\Delta n_e/n_e$ the standard deviation of the fluctuation amplitude. The weighted power transmission function is

$$T_{\text{w}}(n_y) = \int_{-1}^{+1} T(n_y, n_z)\, p(n_z)\, \mathrm{d}n_z \tag{10}$$

RFX-mod discharges are characterized mainly by two classes of density fluctuations: high-frequency fluctuations (≈ 100 kHz) at high amplitude (up to 100%) but with long correlation length ($\lambda_z = 10 \div 20$ cm), and low-frequency fluctuations at lower amplitude ($\approx 10\%$) and with shorter λ_z ($1.5 \div 4.5$ cm) [24]. Figure (5) shows the effects on the conversion efficiency (8) of the density fluctuations with the aforementioned values of correlation lengths in RFX-mod. Thus, from this rough analysis a reduction of the transmission coefficient of 30% can be expected in the worst case of high frequency fluctuations.
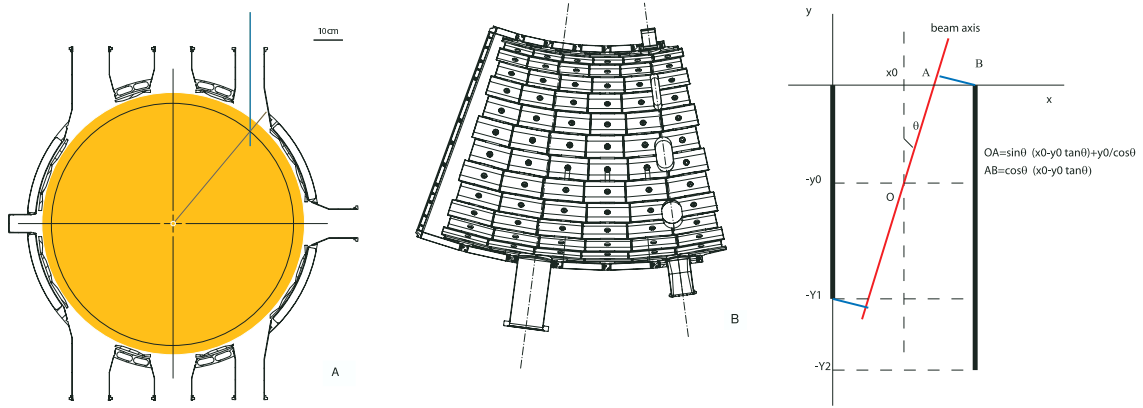
Figure 6. (A) poloidal cross section (B) top-view of RFX-mod with the possible openings for ECRH. In (B) the vertical incidence through the top right port is equivalent to a poloidal entering angle of approximatively 36°. The frame (C) shows a simplified plot of the top right port.

3. O-X-B launch geometry in RFX-mod

Figure (6.A) shows the poloidal cross section of RFX-mod with the possible ports for ECRH. The equatorial port together with the central top/bottom ports are excluded since they do not allow injection at the optimal angle found in Fig. (4). The left (inner) top/bottom openings must be excluded as well, as they are only 3 cm wide in the toroidal direction (see Fig. (6.B)), too small for a beam of realistic diameter ($\approx 4\lambda \approx 4$ cm).

Thus the only possible ports are those on the top and the bottom, on the outward side. To determine the beam waist w_0 (the minimum beam radius) and its position we refer to the sketch in Fig. (6.C). It is important to reduce the power lost on the walls of the port. For a Gaussian beam, the power confined up to a distance w (the beam radius) from the beam axis is $\approx 86\%$ of the total power and it increases to $\approx 96\%$ and $\approx 98\%$ for larger distances, respectively of $1.3\,w$ and $1.5\,w$. In vacuum, the beam radius w evolves according to [25]:

$$w(z) = w_0 \sqrt{1 + \left(\frac{\lambda\, z}{\pi\, w_0^2}\right)^2} \tag{11}$$

with z the distance along the beam axis from the waist position $(x_0, -y_0)$. If z_1 is the distance from $(x_0, -y_0)$ to the port entrance, the first condition to be satisfied is:

$$w(z_1) < \cos\theta\, [x_0 - y_0\, \tan\theta]/1.3 \tag{12}$$

where hereafter we assume that only $\approx 4\%$ of launched power can intercepts the port walls. An equivalent condition must be satisfied to avoid that the beam encounters the port wall on the plasma side,

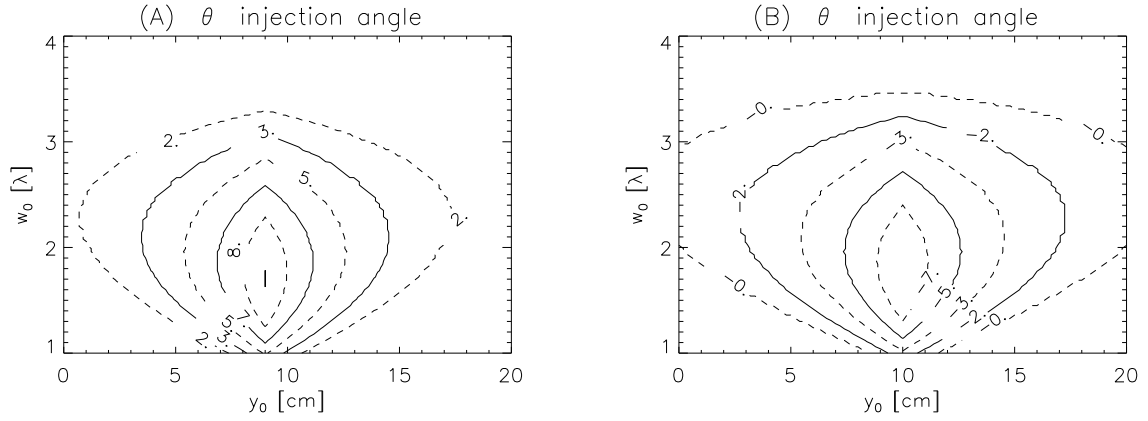$$w(z_2) < \cos\theta\, [x_0 - (y_{\max} - y_0)\, \tan\theta]/1.3 \tag{13}$$

Figure 7. Contour plots of the maximum (A) clockwise (B) counter-clockwise tilt angle θ relative to the port axis (see Fig. 6) as function of the vertical position y_0 and width w_0 of the beam waist. Because of the port wall asymmetry, the clockwise and counterclockwise tilt angles have different values.
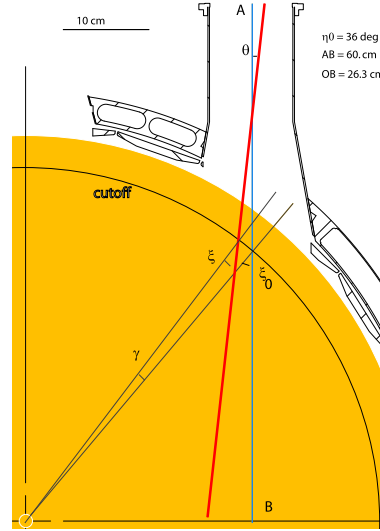

Figure 8. Cross section of the top/external pipe.

The port is evidently asymmetric, with the wall on the right hand side of Fig. (6.C) being longer than that on the left side. This asymmetry translates in a different θ–range between clock– and counter–clockwise. Fig. 7 shows the contour plots of the launching tilt angle θ for RFX-mod port dimensions. A good compromise seems to be

$$1.5\lambda < w_0 < 2.5\,\lambda \tag{14}$$

$$8 \text{ cm} < y_0 < 12 \text{ cm} \tag{15}$$

In Fig. 8 the cross section of the pipe is shown together width the launch geometry. For $\theta = 0$ the beam axis defines an angle η_0 with the normal at the cutoff surface of approximately 36°. However, for $\theta \neq 0$ $\eta = \eta_0 - (\theta \pm \gamma)$ where the signs $+$ and $-$ apply respectively to positive (clockwise) and negative θ (counterclockwise). Fig. 9 shows the incidence angle for a cutoff surface at $x = 0.9\ a$. Thus for $y_0 \approx 9$ cm and $w_0 \approx 1.8\ \lambda$,
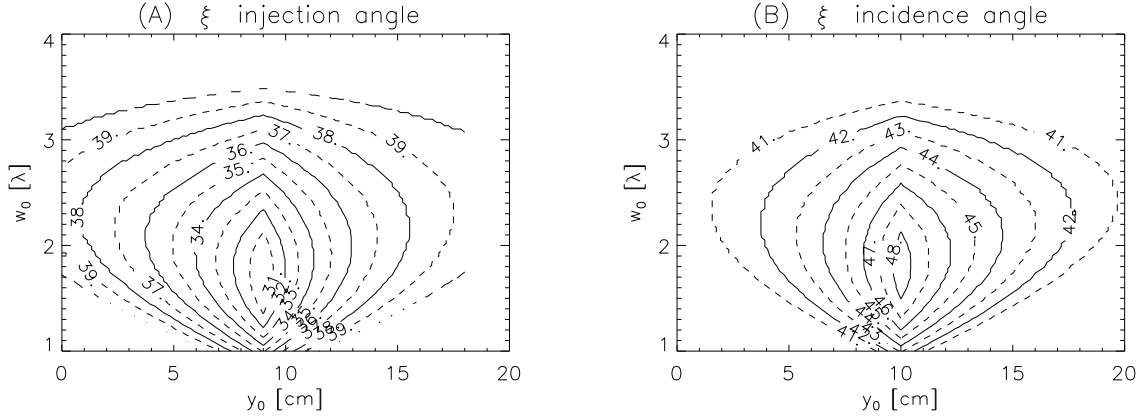
Figure 9. Incidence angle as function of w_0 and y_0 for the case considered in Fig. 7. The cutoff surface has been assumed to lie at $\rho = 0.9$.
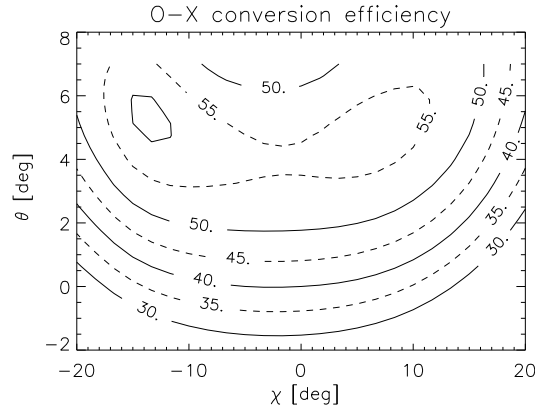

Figure 10. Contour plots of the O-X conversion efficiency: numerical generalization of Fig. (4) to a realistic beam of finite width, $w_0/\lambda = 2.8$.

the incidence angle ranges from 30° to 41°.

4. Mode conversion efficiency of a Gaussian beam

The mode conversion efficiency in 2-dimensional geometry has been calculated with the full-wave finite-difference-time-domain IPF-FDMC (Institut für Plasma Forschung, Finite Difference Mode Conversion) [17] code, which solves the Maxwell's equations

$$\frac{\partial \vec{B}}{\partial t} = -\vec{\nabla} \times \vec{E} \qquad \frac{\partial \vec{E}}{\partial t} = c^2 \vec{\nabla} \times \vec{B} - \frac{1}{\epsilon_0} \vec{J} \qquad (16)$$

in a Cartesian coordinate system. Regarding the constitutive relation, the time-evolution of the plasma current is described in cold plasma approximation by

$$\frac{\partial \vec{J}}{\partial t} = \epsilon_0 \, \omega_{\mathrm{pe}}^2 \vec{E} - \frac{e}{m_e} \vec{J} \times \vec{B} \qquad (17)$$
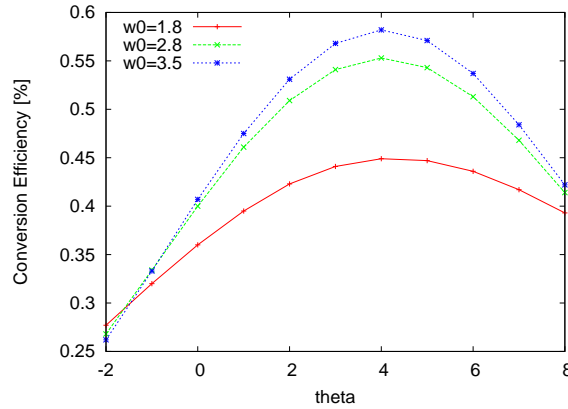
Figure 11. O-X conversion efficiency for three values of the beam waist.

The cold approximation (17) correctly describe the O-X mode conversion and Figure (10) shows the O-X conversion efficiency for the launcher angles considered in the previous section. As already seen in the slab geometry calculation of Fig. (4), the contours of the conversion efficiency are elliptic with different sensitivities to the two angles. The plasma equilibrium considered in Figure (10) is characterised by $\alpha = 5.1, \Theta_0 = 1.47$, $I_p = 1$ MA and $I/N = 7 \cdot 10^{-14}$ A m ($n_0 = 2.5 \cdot 10^{19}$ m^{-3}). An optimal efficiency of 58% is predicted by these simulations. The major cause for conversion efficiency degradation with respect to the slab geometry calculations (Eq. (8) and Fig. (4)) is the mismatching between the curvatures of the beam and the P cutoff layer. This is shown in Fig. (11) for three values of the waist w_0. The narrower the waist, the wider the beam width and curvature at the P cutoff are, which increase the mismatch. To minimize this mismatch, the waist of the beam should be as close as possible to the plasma or even inside the plasma. There are technical limits to this. The lenses used for some diagnostics cannot stand the higher rf power densities.

To describe the X-B mode conversion at the UHR, the cold plasma description has been generalized to include warm plasma corrections [26, 20]. In particular the parallel dispersion is neglected ($k_\parallel^2 v_{\mathrm{th}}^2/\omega^2 = 0$) and only the dominant first-order term in the Larmor radius expansion is considered in the plasma current [27]:

$$\frac{1}{4\pi\varepsilon_0}\vec{J} = \vec{\nabla}_\perp \cdot \left(\sigma \vec{\nabla}_\perp \cdot \vec{E}_\perp\right) - \vec{\nabla}_\perp \times \left(\sigma \vec{\nabla}_\perp \times \vec{E}_\perp\right) \tag{18}$$

with :

$$\sigma = \frac{3}{2}\frac{X}{\left(1 - Y^2\right)\left(1 - 4\,Y^2\right)}\frac{v_{\mathrm{the}}^2}{c^2} . \tag{19}$$

This approximation is correct to quantify the mode conversion coefficients close to the UHR but it lacks of the necessary terms to describe the propagation and absorption as the EB waves propagate away from the UHR towards the cyclotron harmonics.

A damping mechanism is necessary to reach steady-state in simulations, and presently this has been achieved with a numerical viscosity term acting on the EBWs [17].
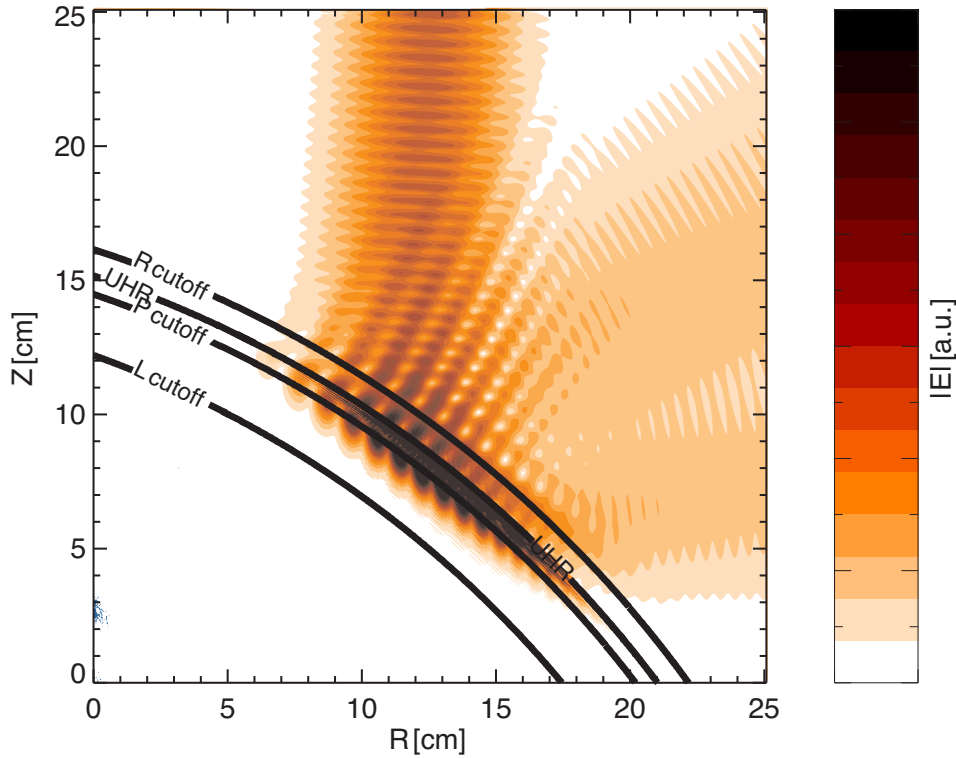
Figure 12. *O-X mode conversion at the P cutoff.*

However, the power deposition is confined in the layer between the UHR and the Doppler shifted $f = 2\,f_{\mathrm{ce}}$ cyclotron harmonic resonance. For the same parameters as in Fig. (10) and an optimal θ launch angle, Fig. (12) shows the conversion O-X at the P cutoff whereas Fig.(13) the X-B conversion at the UHR. In Fig.(13) the EBWs are the waves with very short wavelength and localized close to the UHR. The IPF-FDMC code is suited to deal with density fluctuations, but a detailed analysis is outside the scope of the present paper.

In Fig. (12), obtained with only O-X conversion, a considerable fraction of the injected power is reflected at the conversion layer. Multiple reflections of the reflected power from the vacuum vessel wall (working as a good reflector at this range of frequencies) are expected to increase the amount of power absorbed by the plasma. However, an issue of possible concern is the power reflected back into the launching port: if the geometry of the launching port is included in the calculations the power reflected back into this port can be estimated to $\approx 20\,\%$ of the injected power. Of this reflected power into the port only a small fraction can reach the generator because of geometrical constraints. This must be further investigated and some mitigation must be envisaged.

In absence of a detailed analysis of CD efficiency, according to the experimental dimensionless EBCD efficiency obtained at W7-AS [11] (for $n_e \approx 1.05 \times 10^{20}\,\mathrm{m}^{-3}$ and $T_e \approx 800$ eV), rescaled to the typical densities and temperatures of RFX-mod close to the reversal layer ($n_e \approx 1. \times 10^{19}\,\mathrm{m}^{-3}$ and $T_e \approx 500$ eV) it might be realistic to assume
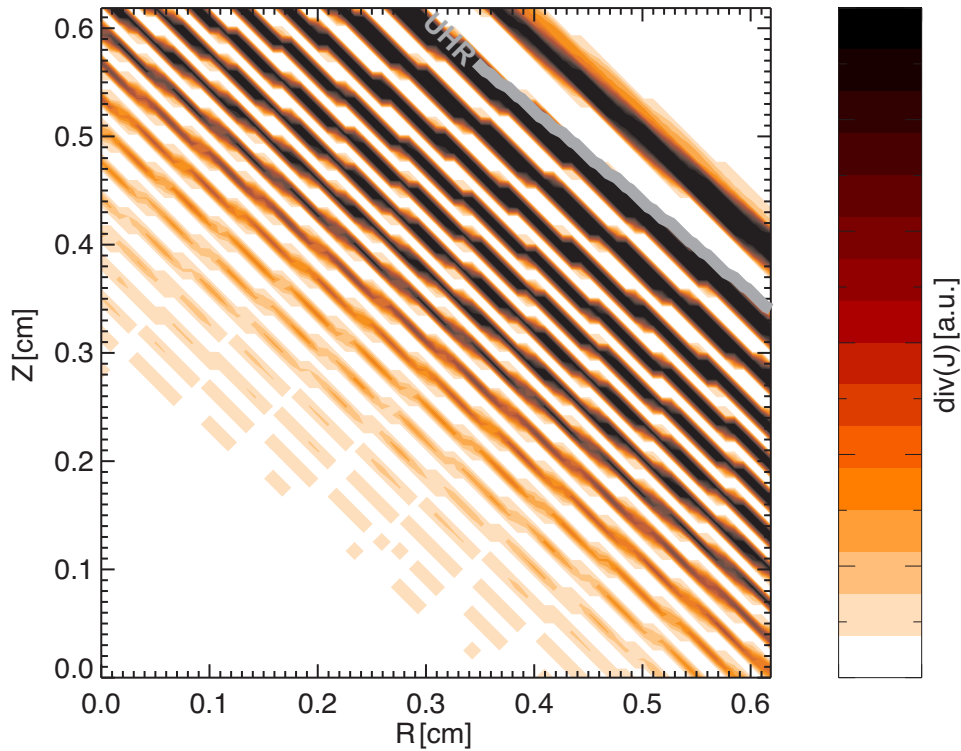
Figure 13. *Detail of the EBWs generated via mode conversion at the UHR in Fig. (12). As EBWs are quasi-electrostatic waves, the patter is clearer when $\nabla \cdot \vec{j}$ is plotted.*

as reference value a driven current of 0.06 kA for each 1 kW of absorbed power. This is expected to be a lower limit of the CD efficiency, since the reduction of the local resistivity due to local EC heating will enhance also the local Ohmic current.

5. Conclusions

The control of poloidal current in RFP plasmas is important for plasma performance improvements. Because of the typical low confining magnetic fields and the overdense nature of RFP plasmas, radio-frequency current drive has generally narrow operational windows in RFPs. However, the recent encouraging EBW heating and current drive results obtained in overdense Stellarators, Tokamaks as well as emission measurements [7] at low power tests in MST [8] has inspired the present feasibility study of EBW current drive in the RFX-mod device. For typical RFX-mod plasmas with plasma currents larger than 1 MA, the typical values of $2 f_{ce}$ are tens of GHz. At these frequencies the direct excitation through X-B mode conversion is jeopardised by the edge evanescence layer, being wider than the vacuum wavelength. On the contrary, the O-X-B scheme seems to offer an acceptable conversion efficiency, calculated with a 2-d full-wave code in real geometry. An important limitation in conversion efficiency is the mismatch between the curvatures of the beam and the P cutoff surface. However, the maximum conversion efficiency obtained is promising and comparable with the

experimental values in Tokamaks and Stellarators. Concerning the power deposition profiles and driven current profiles, a future analysis with ray tracing codes coupled with Fokker-Planck solvers is necessary. So far we have considered not particularly optimistic scaling obtained from standard RFX discharges [28]. If the wave heating and current drive scheme would actually work, favorable effects should be expected, precisely through the improvements of the scalings.

It goes without saying that the fraction of power reflected back towards the launching port can be high if particular care is not paid. Thus in a preliminary phase it would be necessary to work at low EC power and detect with probes the reflected power at different spatial locations.

6. Acknowledgments

[1] R. Paccagnella, S. Ortolani, P. Zanca, A. Alfier, T. Bolzonella, L. Marrelli, M. E. Puiatti, G. Serianni, D. Terranova, M. Valisa, M. Agostini, L. Apolloni, F. Auriemma, F. Bonomo, A. Canton, L. Carraro, R. Cavazzana, M. Cavinato, P. Franz, E. Gazza, L. Grando, P. Innocente, R. Lorenzini, A. Luchetta, G. Manduchi, G. Marchiori, S. Martini, R. Pasqualotto, P. Piovesan, N. Pomaro, P. Scarin, G. Spizzo, M. Spolaore, C. Taliercio, N. Vianello, B. Zaniol, L. Zanotto, and M. Zuin. Active-feedback control of the magnetic boundary for magnetohydrodynamic stabilization of a fusion plasma. *Physical Review Letters*, 97(7):075001, 2006.

[2] T. Bolzonella, P. Martin, S. Martini, L. Marrelli, R. Pasqualotto, and D. Terranova. Quasistationary magnetic fluctuation control in the reversed field pinch: A proof of principle experiment. *Phys. Rev. Lett.*, 87(19):195001, Oct 2001.

[3] J-E Dahlin, J Scheffel, and J K Anderson. Numerical studies of active current profile control in the reversed-field pinch. *Plasma Physics and Controlled Fusion*, 49(2):183–195, 2007.

[4] J Scheffel and J-E Dahlin. Confinement scaling in the advanced reversed-field pinch. *Plasma Physics and Controlled Fusion*, 48(11):L97–L104, 2006.

[5] E. Uchimoto, M. Cekic, R. W. Harvey, C. Litwin, S. C. Prager, J. S. Sarff, and C. R. Sovinec. Lower-hybrid poloidal current drive for fluctuation reduction in a reversed field pinch. *Physics of Plasmas*, 1(11):3517–3519, 1994.

[6] R. Bilato and M. Brambilla. Radio frequency cd by lh waves in the reversed field experiment. volume 485, pages 202–206. AIP, 1999.

[7] P. K. Chattopadhyay, J. K. Anderson, T. M. Biewer, D. Craig, C. B. Forest, R. W. Harvey, and A. P. Smirnov. Electron bernstein wave emission from an overdense reversed field pinch plasma. *Physics of Plasmas*, 9(3):752–755, 2002.

[8] V. Svidzinski M. Cengher, J.K. Anderson and C.B. Forest. Coupling to the electron bernstein wave using a phased array of waveguides in mst reversed field pinch. *Nuclear Fusion*, 46(5):521–531, 2006.

[9] A. G. Litvak, E. V. Suvorov, and M. D. Tokman. On the possibility of current drive in tokamaks by bernstein modes. *Physics Letters A*, 188:64, 1994.

[10] C. B. Forest, P. K. Chattopadhyay, R. W. Harvey, and A. P. Smirnov. Off-midplane launch of electron bernstein waves for current drive in overdense plasmas. *Physics of Plasmas*, 7(5):1352–1355, 2000.

[11] H. P. Laqua, H. Maassberg, N. B. Marushchenko, F. Volpe, A. Weller, and W. Kasparek. Electron-bernstein-wave current drive in an overdense plasma at the wendelstein 7-as stellarator. *Phys. Rev. Lett.*, 90(7):075003, Feb 2003.

[12] F. S. McDermott, G. Bekefi, K. E. Hackett, J. S. Levine, and M. Porkolab. Observation of the parametric decay instability during electron cyclotron resonance heating on the versator ii tokamak. *Physics of Fluids*, 25(9):1488–1490, 1982.

[13] C.B. Forest, R.W. Harvey, and A.P. Smirnov. Power deposition by mode converted electron bernstein waves in the diii-d 'heat pinch' experiments. *Nuclear Fusion*, 41(5):619–623, 2001.

[14] R Wilhelm, V Erckmann, G Janzen, W Kasparek, G Muller, E Rauchle, P G Schuller, K Schworer, and M Thumm. Electron cyclotron resonance heating and confinement in the w vii-a stellarator. *Plasma Physics and Controlled Fusion*, 26(12A):1433–1444, 1984.

[15] H. P. Laqua, V. Erckmann, H. J. Hartfuß, H. Laqua, and W7-AS Team ECRH Group. Resonant and nonresonant electron cyclotron heating at densities above the plasma cutoff by o-x-b mode conversion at the w7-as stellarator. *Phys. Rev. Lett.*, 78(18):3467–3470, May 1997.

[16] A. Mueck, L. Curchod, Y. Camenen, S. Coda, T. P. Goodman, H. P. Laqua, A. Pochelon, L. Porte, and F. Volpe. Demonstration of electron-bernstein-wave heating in a tokamak via o-x-b double-mode conversion. *Physical Review Letters*, 98(17):175004, 2007.

[17] A Köhn, Á Cappa, E Holzhauer, F Castejón, Á Fernández, and U Stroth. Full-wave calculation of the o–x–b mode conversion of gaussian beams in a cylindrical plasma. *Plasma Physics and Controlled Fusion*, 50(8):085018 (17pp), 2008.

[18] P. Innocente, A. Alfier, L. Carraro, R. Lorenzini, R. Pasqualotto, D. Terranova, and the RFX Team.

Transport and confinement studies in the rfx-mod reversed-field pinch experiment. *Nuclear Fusion*, 47(9):1092–1100, 2007.

[19] V. Antoni, D. Merlin, S. Ortolani, and R. Paccagnella. Mhd stability analysis of force–free reversed field pinch configurations. 26(12):1711, 1986.

[20] A. K. Ram and S. D. Schultz. Excitation, propagation, and damping of electron bernstein waves in tokamaks. *Physics of Plasmas*, 7(10):4084–4094, 2000.

[21] D. Gregoratto, L. Garzotti, P. Innocente, S. Martini, and A. Canton. Behaviour of electron density profiles and particle transport analysis in the rfx reversed field pinch. *Nuclear Fusion*, 38(8):1199–1213, 1998.

[22] J. Preinhaelter and V. Kopecky. Penetration of high-frequency waves into a weakly inhomogeneous magnetized plasma at oblique incidence and their transformation to bernstein modes. *J. Plasma Physics*, 10:1, 1973.

[23] E. Mjolhus. Coupling to z mode near critical angle. *J. Plasma Physics*, 31:7, 1984.

[24] P. Scarin, M. Agostini, R. Cavazzana, F. Sattin, G. Serianni, and N. Vianello. Edge turbulence in rfx-mod virtual-shell discharges. *Journal of Nuclear Materials*, 363-365:669, 2007.

[25] Paul f. Goldsmith. *Quasioptical Systems*. IEEE Press, 1997.

[26] Marco Brambilla. *Kinetic Theory of Plasma Waves*. Oxford University Press, USA, 1998.

[27] M Brambilla. Finite larmor radius wave equations in tokamak plasmas in the ion cyclotron frequency range. *Plasma Physics and Controlled Fusion*, 31(5):723–757, 1989.

[28] J. Scheffel and D. D. Schnack. Confinement scaling laws for the conventional reversed-field pinch. *Phys. Rev. Lett.*, 85(2):322–325, Jul 2000.